

# Scanning tunneling microscopy current from localized basis orbital density functional theory

Alexander Gustafsson<sup>1,\*</sup> and Magnus Paulsson<sup>1,†</sup>

<sup>1</sup>*Department of Physics, Linnaeus University, 391 82 Kalmar, Sweden*

(Dated: December 3, 2015)

We present a method capable of calculating elastic scanning tunneling microscopy (STM) currents from localized atomic orbital density functional theory (DFT). To overcome the poor accuracy of the localized orbital description of the wave functions far away from the atoms, we propagate the wave functions, using the total DFT potential. From the propagated wave functions, the Bardeen's perturbative approach provides the tunneling current. To illustrate the method we investigate carbon monoxide adsorbed on a Cu(111) surface and recover the depression/protrusion observed experimentally with normal/CO-functionalized STM tips. The theory furthermore allows us to discuss the significance of *s*- and *p*-wave tips.

PACS numbers: 68.37.Ef, 33.20.Tp, 68.35.Ja, 68.43.Pq

## I. INTRODUCTION

Scanning tunneling microscopy has made large strides since its conception 35 years ago. Advances include studies of detailed atomic structure including the shapes of molecular orbitals<sup>1</sup>, atomic manipulation<sup>2</sup>, and inelastic spectroscopy from vibrational<sup>3</sup> and magnetic excitations<sup>4</sup>. Theoretically, the standard methods of Bardeen<sup>5</sup> and the Tersoff-Hamann<sup>6</sup> approximation have served to model and provide understanding of the STM measurements. The Tersoff-Hamann approach to model STM experiments from first principles calculations has provided a clear understanding of many phenomena<sup>7</sup>. However, with the emergence of non *s*-wave functionalized STM tips<sup>1</sup>, e.g., CO functionalized tip, the Bardeen method with a proper description of the tip states is required<sup>8–11</sup>. Using non-equilibrium Green's function methods advances in the related field of conduction through nanoscale devices has made great progress. However, these methods are in practice not directly applicable to STM modelling since (i) scanning the STM tip over the surface results in many costly computations, and (ii) the prevalence of localized basis set DFT calculations to describe the electronic structure, which cannot accurately capture the tunneling at large distances. These difficulties to use large scale DFT calculations with localized basis set to model STM images has given rise to several methods to improve the modeling capabilities<sup>8,9</sup>. In this work we pursue a similar methodology as Paz *et al.*<sup>8</sup> where the electronic states of the tip and sample sides are calculated accurately close to the tip and sample sides and then propagated in the vacuum region to provide accurate states to use in the Bardeen formalism. However, instead of assuming a flat potential in the vacuum region we utilize the total DFT potential landscape to propagate the wave functions into

the vacuum region and thereby, by the Bardeen method, construct first principles STM images. To benchmark our method, we focus on describing the current dip over a carbon monoxide molecule (CO) adsorbed on the Cu(111) surface<sup>12</sup>, which has been well studied experimentally as well as being used to provide larger resolution when the STM tip is functionalized by the CO molecule<sup>13</sup>.

## II. THEORY

Our theoretical framework relies on the well known Bardeen<sup>5</sup> approximation. In the small current limit, time-dependent perturbation theory using a Fermi's golden rule like formalism, alternatively non-equilibrium Green's function theory<sup>14</sup>, gives the tunneling current as:

$$I = \frac{2\pi e}{\hbar} \sum_{t,s} [f(\varepsilon_t) - f(\varepsilon_s)] |M_{ts}|^2 \delta(\varepsilon_t - \varepsilon_s + eV), \quad (1)$$

where  $f(\varepsilon_{t,s})$  are the Fermi-Dirac functions,  $\varepsilon_{t,s}$  the energy levels of tip and substrate relative respective chemical potential, and  $V$  the applied bias. The matrix elements  $M_{ts}$  couples the tip states,  $\varphi_t$ , to the substrate states,  $\varphi_s$ , by the following expression:

$$M_{ts} = -\frac{\hbar^2}{2m} \int_S dS \cdot [\varphi_t^*(\mathbf{r}) \nabla \varphi_s(\mathbf{r}) - \varphi_s(\mathbf{r}) \nabla \varphi_t^*(\mathbf{r})], \quad (2)$$

where the integral is evaluated on any surface in between the adsorbate and tip. In this article, we focus on the low bias conductance, where only the tip and substrate wave functions close to the Fermi energy are needed. Generalizations to investigate bias dependent tunneling should be straightforward. Since the integration surface is far from either the tip or substrate, the low electron density in addition to the use of finite range basis or-

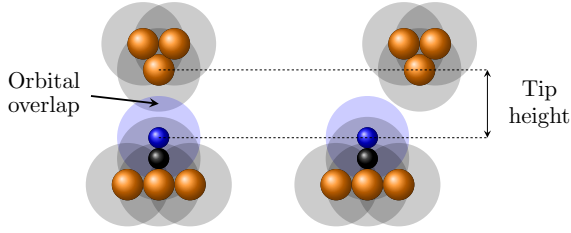


FIG. 1: Illustration of CO adsorbed on a Cu surface and Cu tip. The finite range basis orbitals used in SIESTA, shaded region, underline the difficulty of describing the tunneling current with a localized basis.

bitals in SIESTA, c.f., Fig. 1, the wave functions are poorly described in the vacuum region. In contrast, the wave functions close to the atomic nuclei can be accurately and efficiently calculated by SIESTA. STM images can thus be calculated by propagating these accurate wave functions close to the nuclei into the vacuum region.

#### A. Propagation of wavefunctions

The SIESTA method solves the Kohn-Sham equations using norm conserving pseudopotentials and a localized basis set. Outside the range of the pseudopotentials, the Kohn-Sham orbitals obey, at a specified energy, a Schrödinger like equation with a local potential which makes it conceptually straightforward to propagate a known wave function from a surface into the vacuum region. The substrate and tip sides are treated in the same way, and to simplify the presentation we only describe the substrate side in the following. To propagate the wave functions in real space, we start from a charge density iso-surface, see Fig. 2, chosen close to the substrate but outside of the radii of the pseudopotentials. In the vacuum region, the Kohn-Sham equations (Rydberg units) therefore reads  $(-\nabla^2 + V_{\text{tot}})\Psi = \varepsilon_F \Psi$  where the total potential ( $V_{\text{tot}}$ ) contains the Coulomb, Hartree, and exchange-correlation terms. For efficiency, the calculation cell actually contains both substrate and tip situated far enough away from each other to give a negligible current. To remove the tip potential we therefore find the maximum  $V_{\text{tot}}$  in the vacuum region and set the total potential further away from the substrate to the average value of  $V_{\text{tot}}$  at that height above the substrate. This requires a sufficiently large vacuum gap in order to capture the work function properly.

The substrate and tip states are obtained for the device region coupled to semi-infinite electrodes using TRANSIESTA<sup>18</sup>, i.e., non-equilibrium Green's function method built on the SIESTA method. The states at the Fermi energy are found

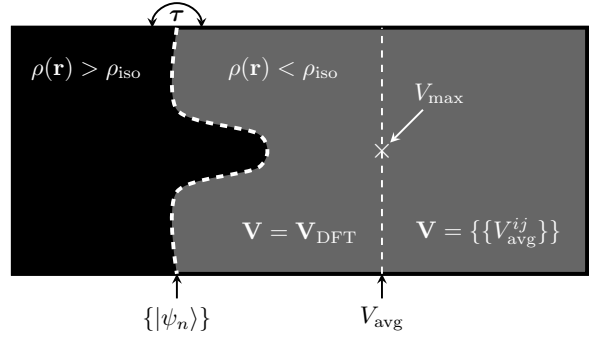


FIG. 2: 2D illustration of the device (full region), substrate (black) and vacuum (gray) regions. The dashed white line illustrates the constant density surface,  $\rho_{\text{iso}}$  from which the substrate states,  $\{|\psi_n\rangle\}$ , are propagated into the vacuum region.

in the SIESTA basis set by diagonalizing the partial spectral function<sup>15</sup>, i.e., the spectral function of the substrate (tip) side  $A_{s(t)} = G_d \Gamma_{s(t)} G_d^\dagger = \sum_n |\tilde{\psi}_n\rangle \lambda_n \langle \tilde{\psi}_n|$ , where  $G_d$  is the retarded Green's function of the device region, and  $\Gamma_{s(t)}$  is the broadening of the substrate (tip). Although the device region can be arbitrarily large, only a few (of the order of 10 in our examples) eigenvalues are non-zero and the corresponding eigenvectors give the scattering states when properly normalized<sup>15</sup>,

$$|\psi_n\rangle = \sqrt{\frac{\lambda_n}{2\pi}} |\tilde{\psi}_n\rangle, \quad (3)$$

where  $|\psi_n\rangle$  are the energy normalized eigenvectors. To propagate these states into the vacuum region, the wave functions are evaluated on the same real space grid as used by SIESTA.

The real space wave functions can then be computed using the Green's function formalism. Here we use the finite difference method to discretise the device region<sup>23</sup>, i.e., the gray and black regions in Fig. 2. By means of the Dyson equation, the propagated modes in the vacuum region (gray region) are described by

$$|\varphi_n\rangle = \mathbf{G}_0 \boldsymbol{\tau} |\psi_n\rangle, \quad (4)$$

where  $\mathbf{G}_0 = (\varepsilon_F \mathbf{I} - \mathbf{H}_d - \boldsymbol{\Sigma}_R)^{-1}$  is the isolated Green's function of the vacuum region optionally connected to a semi-infinite continuation on the right hand side  $\boldsymbol{\Sigma}_R$ , and  $\boldsymbol{\tau}$  is the coupling matrix between the substrate and the vacuum region. The Hamiltonian that occurs in the isolated Green's function contains the finite difference Laplacian and the total potential,  $V_{\text{tot}}$ , extracted from DFT. The total potential and charge density are readily available in real space from the SIESTA code and we therefore only need to specify the boundary conditions to be able to propagate the wave

functions. Furthermore, calculation of the self-energy on the vacuum boundary,  $\Sigma_R$ , can safely be omitted if the device region is large, since the propagated modes vanish exponentially fast in the vacuum region (i.e., total reflection). Inclusion of the vacuum self-energy is therefore optional as long as the device region is large enough, and will be omitted in the following. We compute the modes in the vacuum region,  $|\varphi_n\rangle$ , by solving the (sparse) linear system of equations,

$$(\varepsilon_F \mathbf{I} - \mathbf{H}_d) |\varphi_n\rangle = \boldsymbol{\tau} |\psi_n\rangle, \quad (5)$$

where  $\mathbf{H}_d$  contains all elements of the vacuum region (gray region outside the isosurface in Fig. 2), and the previously modified DFT potential. Note that solving the system of linear equations is much less demanding than performing a matrix inversion to obtain  $\mathbf{G}_0$ , allowing for larger systems to be considered.

Assuming that the calculated wave functions are unchanged by translation of the tip relative the substrate allows us to efficiently calculate the STM current image as a convolution:

$$M_{ts}(\mathbf{R}) = -\frac{\hbar^2}{2m} \int_S dS \cdot [\varphi_t^*(\mathbf{r} + \mathbf{R}) \nabla \varphi_s(\mathbf{r}) - \varphi_s(\mathbf{r}) \nabla \varphi_t^*(\mathbf{r} + \mathbf{R})], \quad (6)$$

where the convolution is performed efficiently using Fast Fourier Transforms (FFT).

### B. Computational details

We use the SIESTA<sup>16</sup> DFT program to obtain the relaxed geometry of the supercell. The substrate consists of five  $4 \times 4$  Cu-layers forming the Cu(111) geometry, with lattice constant 2.57 Å hence giving images of dimensions  $10.3 \times 10.3$  Å. The molecule, the two top layers of the substrate, and the tip atom are relaxed until the residual force is less than 0.04 eV/Å. The tip consists of three similar layers with a pyramidal tip apex with four Cu-atoms attached to the underside of the tip slab. The maximal range of the atomic orbitals are 4.8, 3.0 and 3.9 Å for Cu, O, and C respectively. Periodic boundary conditions are imposed in all spatial dimensions. The computations were performed with the PBE GGA functional<sup>17</sup>, SZP(DZP) basis set for Cu(CO), a 400 Ry mesh cut-off energy for real space grid integration, and  $4 \times 4$   $k$ -points along the surface plane. Non-equilibrium wave functions are calculated by the TRANSIESTA<sup>18</sup> and INELASTICA<sup>19</sup> modules by adding three(six) layer electrodes at the substrate(tip) side of the supercell.

For the real space wave function propagation we have found that the real space grid given by

SIESTA (200 Ry cutoff) is unnecessary fine, and in the wave function propagation the grid coarseness were doubled (corresponding to a 50 Ry cutoff in SIESTA). The typical grid sizes used below consists of  $40 \times 40$  points in the plane of the substrate and approximately 50 points along the transport direction. The density on the isosurface,  $\rho_{\text{iso}}$ , is chosen so that the this surface lies just outside the radii of the pseudopotentials, in the following we will use  $\rho_{\text{iso}} = 5 \times 10^{-3} (\text{Bohr})^{-3}$ , and we have verified that small changes in this parameter do not affect the results. For the STM image calculations only the wave functions in the  $\Gamma$ -point were considered.

## III. RESULTS

We demonstrate the theory by primary considering the system where a CO molecule is adsorbed on a top site of a clean  $4 \times 4$  atom Cu(111) surface with a pyramidal shaped tip apex, consisting of four copper atoms, see Fig. 1. A comparison between direct use of the orbitals computed from the localized SIESTA basis, and the modes found by Eq. (5) will first be examined to highlight the advantages of our theory. This reveals the characteristic depression over the CO-molecule in the tunneling current, which will be analysed in terms of the individual wave functions, and compared with the STM image obtained with a CO terminated tip. The tip-height is henceforth defined as the core-core height difference (along  $\hat{z}$ ) between the outermost tip apex atom and its closest atom adsorbed on the substrate, see Fig. 1.

### A. Comparison between localized and propagated wave functions

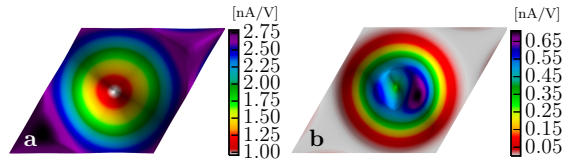


FIG. 3: Comparison of the calculated constant height STM image at 5.0 Å, computed by means of a) the propagated, and b) SIESTA wave functions.

To illustrate the limitations of using the localized orbitals to describe the wave functions in the vacuum gap, we use Eq. (1) for both the wave functions found directly from SIESTA and compare with using the propagated modes. Fig. 3 present the constant tip-height (5.0 Å) tunneling current showing the expected dip in current over

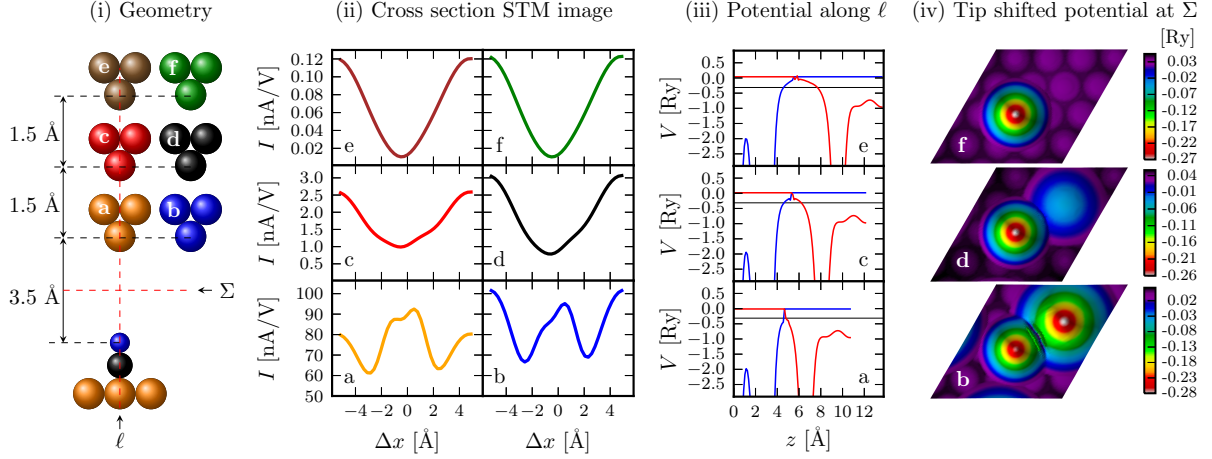


FIG. 4: STM image dependence on the substrate-tip distance and lateral displacement of the tip. (i) Illustrations of the six different geometries. (ii) Constant height STM image cross sections for the six geometries. (iii) total potential energy along the bonding axis of the CO molecule where the blue (red) line is the potential used in propagation of the wave functions from the substrate (tip) side, and the horizontal black line is the Fermi energy. (iv) the total potential at the surface  $\Sigma$  in (i).

the CO molecule using the propagated wave functions (Fig. 3 a) and the failure of the SIESTA wave functions to reproduce the dip (Fig. 3 b).

For the SIESTA wave functions, the vanishingly small current away from the molecule is a consequence of the vanishing overlap between the tip and substrate as the basis orbitals barely overlap. The CO molecule therefore appears as a protrusion in the tunneling current contrary to the characteristic dip seen experimentally. By propagating the SIESTA wave functions into the vacuum region provides an overall increase in the tunneling current, and additionally, the characteristic dip over the CO molecule is recovered.

### B. Substrate-tip distance

The basic assumption in the Bardeen approximation is that the potential of the tip do not perturb the wave functions from the substrate and vice versa<sup>5</sup>. To investigate this assumption we carried out calculations at 3 different substrate-tip distances with the tip above the CO molecule and with the tip laterally displaced from the molecule, see Fig. 4 (i).

Visualizing the DFT total potential at a constant height above the substrate, see Fig. 4 (iv), clearly shows the effect of the tip on the potential at substrate-tip distances below 5 Å, e.g., Fig. 4 (iv) (f) shows the potential of the molecule and underlying Cu lattice while (d) and (b) clearly shows the perturbation of the potential from the tip. The perturbation of the tip potential on the substrate wave functions severely modify the simulated STM

images for distances below 5 Å, see Fig. 4 (ii), and gives differences between the calculated STM images even when the tip is shifted laterally at the same height. Furthermore, the approximation to use a flat potential outside the maximum potential, see Fig. 4 (iii) is also questionable for substrate-tip distances below 5 Å since the height of the potential will give the exponential decay into the vacuum region.

In summary, these calculations demonstrate the need for a relatively large vacuum gap in order to minimize the impact from the tip potential when calculating the substrate wave functions and vice versa. In the following calculations we keep the substrate-tip distance larger than 5 Å. However, this might, in some cases, be an artificially large distance when comparing with experimental STM images. Other possible solutions might be to introduce the tip potential as a perturbation although this would necessitate the recalculation of the perturbed wave functions at each lateral displacement of the tip.

### C. Wave function analysis

To gain further insights of the tunneling current contributions to the constant height STM image, it is instructive to look at the various propagated wave functions at the surface on which the integral,  $M_{ts}$ , c.f., Eq. (2), is evaluated, see Fig. 5. The gradients in the integral can, to zeroth order, be approximated by an exponential decay in the  $\hat{z}$  direction, which means that the the integral  $M_{ts}$  is proportional to the overlap of the wave func-

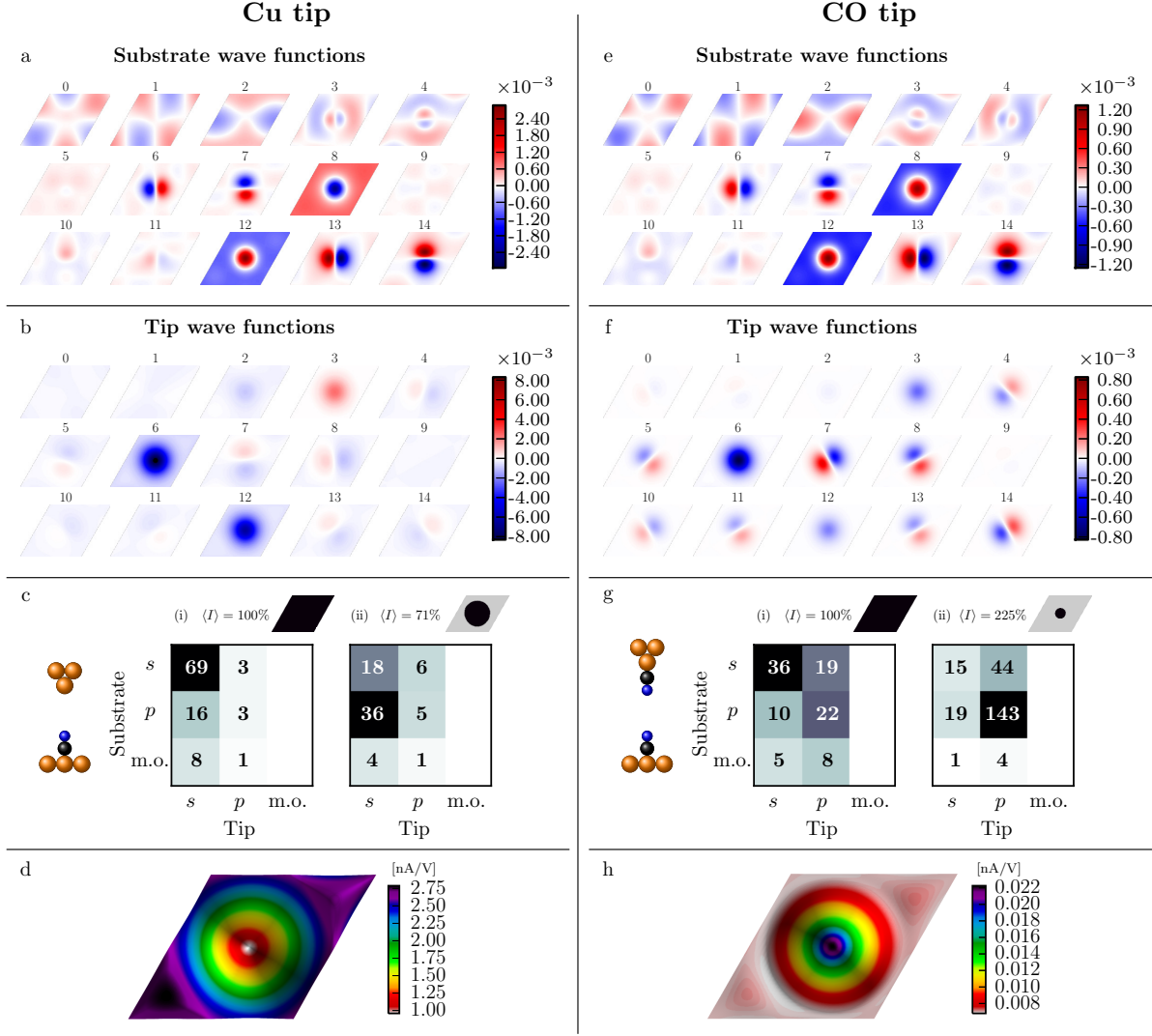


FIG. 5: Left column (a, b, c, and d) shows the real part of the substrate and tip wave function amplitudes for the pyramidal copper ( $s$ -wave) tip, evaluated in the centre of the vacuum region ( $5.0 \text{ \AA}$  tip-height). The matrix in c shows the average tunneling current for the  $s$ -,  $p$ -, and miscellaneous orbital (m.o.) combinations. The average is taken over tip positions over (i) the full cell and (ii) the area over the molecule, see text. Figure (d) shows the resulting constant height STM image. The right column (e, f, g, and h) shows the results with a CO functionalized ( $p$ -wave) tip at  $5.2 \text{ \AA}$  tip-height.

tions on the integration surface. To separate the contributions from the different types of channels we further separate the contributions of  $s$ -, and  $p$ -type orbitals from the substrate and tip. These contributions vary with the tip-position and we therefore present the average with respect to tip position over the full image or over the molecule, i.e.,  $\left\langle \sum_{s,t \in \{s,p,m.o\}} |M_{ts}|^2 \right\rangle_A$ , where the area  $A$  is either the full image, or the region delimited by the half way between the maximum and minimum current. The resulting plot of the  $|M_{ts}|^2$  matrix, see Fig. 5, separates the contributions from the  $s$ - and  $p$ -wave states and allows us to discuss

the origin of the STM contrast.

### 1. Origin of the current dip

For the Cu terminated tip, the main tunneling current (69%) originates from a few  $s$ -like orbitals from both substrate (mainly states 8 and 12) and tip side (6 and 12), see left part of Fig. 5 c), whereas, the  $p$ -wave orbitals play a minor role. We further note that the tip and substrate states contributing to the current (substrate states 8 and 12 and tip states 6 and 12) are virtually identical apart from a constant. It seems likely that a



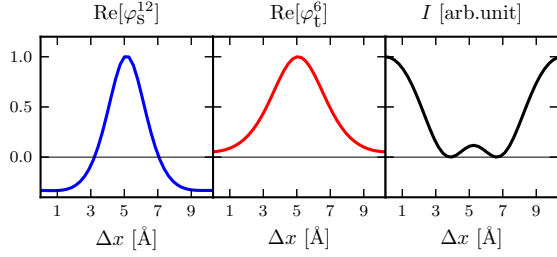


FIG. 6: Left and middle figure shows the most conducting substrate and tip wave function combination in a cross section profile over the CO molecule, and the right figure displays a cross section profile of the STM current originating from these two states. Peak heights are normalized.

unitary transformation of the wave functions can provide an even simpler picture where the main current is carried by a single state substrate and tip state, c.f., current eigenchannels<sup>15</sup>.

The average of the current and current matrix over the central area close to the molecule shows a clear decrease in the average current, see Fig. 5 (c) right. The main part of the current is still carried through the  $s$ -wave tip states although the current going through the substrate  $s$ -wave decrease substantially and the importance of the  $p$ -waves increase markedly. As neither the amplitude, nor the sign of the wave functions are clearly visible in Fig. 5, a cross section of the most transmitting mode combination is shown in Fig. 6. This combination, i.e.,  $\{|\varphi_s^{12}\rangle, |\varphi_t^6\rangle\}$  (giving 24% of the total tunneling current), reveals a sign change for the substrate mode, whereas the sign is strictly positive for the tip mode. The sign change implies that the overlap of the wave functions decrease when the tip is centered over the molecule and gives, as an interference effect, the dip in tunneling current, see Fig. 6. Alternatively this may be interpreted using the Tersoff-Hamann approximation<sup>6</sup>, or the more general Chen's derivative rules<sup>20</sup>, where for an  $s$ -wave tip the current is simply given by the local density of states (LDOS) at the tip position, see Fig. 7. Note that the LDOS as distances below  $\sim 5$  Å are not directly relevant for the STM image as we should examine the LDOS at the tip position.

## 2. CO-terminated tip

Using a CO-terminated tip increases the importance of the tip  $p$ -orbitals and can increase the STM resolution<sup>1,21,22</sup>. Previous studies have introduced  $p$ -wave tips in an approximate fashion where the mix between tip  $s$ - and  $p$ -waves were set by

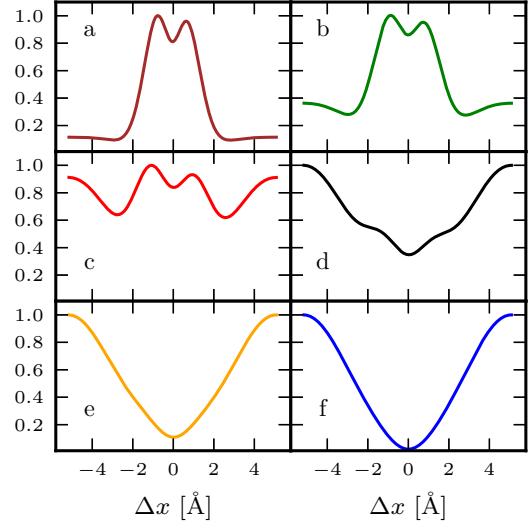


FIG. 7: Cross section profiles of the normalized local density of states from the substrate/molecule at distances  $z = (2.5, 3.4, 4.3, 5.2, 6.1, 7.0)$  Å in (a,b,c,d,e,f).

hand<sup>1</sup>. In addition, the importance of the  $p$ -wave for the CO-functionalized tip has been seen theoretically in calculations of inelastic electron tunneling spectra<sup>21,22</sup>. In our case, the current matrix analysis allows us to analyse the contributions directly from the DFT-calculations of the tip and substrate states.

For the CO-terminated tip our calculations show the reversal of the STM contrast with a conductance peak above the CO molecule in agreement with experiments<sup>13</sup>. The propagated wave functions and the current contributions from the  $s$ - and  $p$ -wave orbitals are shown in the right column in Fig. 5. As with the Cu tip, the various combinations of  $s$ -waves yield a current dip. However, the relative intensity for these  $s$ -waves are significantly weaker for the CO tip, whereas the  $p$ -wave intensities play a dominant role, especially over the molecule, as seen from the current matrix. Away from the molecule, the  $p$ -channels are not as dominant but still significant in the resulting STM current. For the  $p$ -wave tip states, the overlap with the substrate states increase when the substrate states change sign, c.f., Chen's derivative rules for  $p$ -wave tips<sup>20</sup>. The resulting contrast with a conductance peak over the molecule can therefore be understood as the non-cancellation of the overlap between the  $p$ -waves from the substrate and tip.

#### IV. SUMMARY

The ability to propagate the wave functions into the vacuum gap overcomes the disadvantages of localized atomic orbital DFT in describing the wave functions in the STM gap. This allows us to use computationally relatively inexpensive DFT calculations to model STM experiments. The method can furthermore be extended to include  $k$ -point sampling, as well as energy dependence to model scanning tunneling spectroscopy. The usefulness of the method is exemplified by the correct description of the CO molecule (on Cu(111)) depression seen in STM experiments. Here, the depression stems from the sign change of the substrate

wave functions. In contrast, the same molecule shows a protrusion when measured with a CO-functionalized tip which is due to the  $p$ -wave character of the tip.

#### V. ACKNOWLEDGEMENT

We are deeply indebted to Norio Okabayashi and Franz Giessibl for valuable discussions. The computations were performed on resources provided by the Swedish National Infrastructure for Computing (SNIC) at Lunarc. A.G. and M.P. are supported by a grant from the Swedish Research Council (621-2010-3762).

---

\* Electronic address: [alexander.gustafsson@lnu.se](mailto:alexander.gustafsson@lnu.se)

† Electronic address: [magnus.paulsson@lnu.se](mailto:magnus.paulsson@lnu.se)

- <sup>1</sup> L. Gross, N. Moll, F. Mohn, A. Curioni, G. Meyer, F. Hanke, and M. Persson, Phys. Rev. Lett. **107**, 086101 (2011).
- <sup>2</sup> D. M. Eigler and E. K. Schweizer, Nature **344**, 524 (1990).
- <sup>3</sup> B. C. Stipe, M. A. Rezaei, and W. Ho, Science **280**, 1732 (1998).
- <sup>4</sup> C. F. Hijibehedin, C.-Y. Lin, A. F. Otte, M. Ternes, C. P. Lutz, B. A. Jones, and A. J. Heinrich, Science **317**, 1199 (2007).
- <sup>5</sup> J. Bardeen, Phys. Rev. Lett. **6**, 57 (1960).
- <sup>6</sup> J. Tersoff and D. R. Hamann, Phys. Rev. B **31**, 805 (1985).
- <sup>7</sup> B. Persson and H. Ueba, Surf. Sci. **502-503**, 18 (2002).
- <sup>8</sup> O. Paz and J. M. Soler, Phys. Status Solidi B **243**, 1080 (2006).
- <sup>9</sup> E. Rossen and C. F. J. Filipse, Phys. Rev. B **87**, 235412 (2013).
- <sup>10</sup> M.-L. Bocquet and P. Sautet, Surf. Sci. **360**, 128 (1996).
- <sup>11</sup> G. Teobaldi, M. Penalba, A. Arnau, N. Lorente, and W. A. Hofer, Phys. Rev. B **76**, 235407 (2007).
- <sup>12</sup> A. J. Heinrich, C. P. Lutz, J. A. Gupta, and D. M. Eigler, Science **298**, 1381 (2002).
- <sup>13</sup> L. Bartels, G. Meyer, and K.-H. Rieder, Appl. Phys. Lett. **71**, 213 (1997).
- <sup>14</sup> J. B. Pendry, A. B. Pretre, and B. C. H. Krutzen, J. Phys.: Condens. Matter **3**, 4313 (1991).
- <sup>15</sup> M. Paulsson and M. Brandbyge, Phys. Rev. B **76**, 115117 (2007).
- <sup>16</sup> J. M. Soler, E. Artacho, J. D. Gale, A. García, J. Junquera, P. Ordejón, and D. Sánchez-Portal, J. Phys.: Condens. Matter **14**, 2745 (2002).
- <sup>17</sup> J. P. Perdew, K. Burke, and M. Ernzerhof, Phys. Rev. Lett. **77**, 3865 (1996).
- <sup>18</sup> M. Brandbyge, J.-L. Mozos, P. Ordejón, J. Taylor, and K. Stokbro, Phys. Rev. B **65**, 165401 (2002).
- <sup>19</sup> T. Frederiksen, M. Paulsson, M. Brandbyge, and A.-P. Jauho, Phys. Rev. B **75**, 205413 (2007).
- <sup>20</sup> C. J. Chen, Phys. Rev. B **42**, 8840 (1990).
- <sup>21</sup> A. Garcia-Lekue, D. Sanchez-Portal, A. Arnau, and T. Frederiksen, Phys. Rev. B **83**, 155417 (2011).
- <sup>22</sup> M. Paulsson, T. Frederiksen, H. Ueba, N. Lorente, and M. Brandbyge, Phys. Rev. Lett. **100**, 226604 (2008).
- <sup>23</sup> A version using the finite element method is under development.